

Influence of relative permeability on injection pressure and plume configuration during CO₂ injections in a mafic reservoir

Ryan M. Pollyea

Department of Geosciences, Virginia Polytechnic Institute and State University, Blacksburg, VA, United States



ARTICLE INFO

Article history:

Received 25 September 2015

Received in revised form 9 December 2015

Accepted 14 December 2015

Keywords:

Relative permeability

Phase interference

CO₂ sequestration

Injection pressure

Reservoir geomechanics

ABSTRACT

Carbon capture and sequestration projects have traditionally targeted deep sedimentary basins; however, mafic reservoirs may also be attractive targets for CO₂ disposal on the basis of permanent mineral trapping over relatively short time scales (10¹ to 10² yr). Nevertheless, CCS development in mafic reservoirs is hampered by substantial uncertainty in fracture-controlled reservoir characteristics, particularly with respect to the effects of multi-phase fluid flow, e.g., relative permeability and capillary pressure. The present study quantifies uncertainty surrounding relative permeability effects in a basalt reservoir by developing a numerical modeling experiment on the basis of site characterization data from the Slack Canyon #2 flow top, which is one of three flow tops comprising the injection zone at the Wallula Basalt Sequestration Pilot Project in southeast Washington State. This numerical modeling experiment controls for the effects of curvature in the relative permeability models by performing an ensemble of 399 CO₂ injection simulations with constant geometry and reservoir properties, while systematically varying the phase interference parameter (λ) and residual CO₂ saturation (S_{gr}), which govern wetting and non-wetting phase relative permeability, respectively. The relative permeability parameter space is defined by selecting combinations of λ and S_{gr} that cover a wide range of experimental laboratory measurements. For each simulation, CO₂ is injected into the reservoir for 10 years at a constant rate of 2.78 kg s⁻¹ (87,856 metric tons (MT) yr⁻¹), which is 10% of the annual injection rate proposed for one injection scenario at the Wallula Site. Results from the ensemble of simulations show that relative permeability alone can account for >50 MPa of variability in the injection pressure and a two-fold difference in lateral CO₂ plume migration. Additionally, this work shows that curvature in the wetting phase relative permeability model is the stronger influence on reservoir pressure accumulation, while curvature in the non-wetting phase relative permeability model strongly governs CO₂ plume geometry.

© 2015 Elsevier Ltd. All rights reserved.

1. Introduction

In 2014, the Global Carbon Capture and Sequestration Institute reported 22 large-scale carbon capture and sequestration (CCS) projects in operation or under construction worldwide with an additional 14 large-scale projects in the advanced planning stages (GCCSI, 2014). This represents a doubling of industrial-scale CCS deployments since the beginning of decade, and suggests that CCS technology is rapidly maturing from feasibility and pilot stages to full-scale deployment. The primary target formations for geologic CO₂ disposal are deep sedimentary basins, where CO₂ injected in the supercritical phase is readily accepted by high permeability sandstone or carbonate reservoir rock, while low permeability cap rocks, such as shale, inhibit upward migration of CO₂ out of the disposal reservoir (NETL, 2010).

Although widespread CCS development has traditionally focused on sedimentary basins, there is mounting evidence suggesting that mafic reservoirs may also be attractive targets for

geologic CO₂ disposal. The motivation for CCS in mafic reservoirs is based upon laboratory experiments demonstrating favorable water-rock-CO₂ reaction kinetics, which result in permanent CO₂ trapping through Mg dissolution followed by carbonate mineralization (Matter and Kelemen, 2009). For example, Goff and Lackner (1998) and Alexander et al. (2007) utilized acid-dissolution experiments to propose acid leaching treatments as a means to enhance Mg dissolution, thus increasing the mineralization potential in peridotite and serpentine. In addition, Wang and Giamar (2012) showed increasing Mg dissolution with increasing salinity in batch experiments reacting CO₂ with forsterite. Similarly, Kelley et al. (2001) found carbonate mineralization in a Mid-Atlantic Ridge hydrothermal vent field composed of peridotite, suggesting that CO₂ mineralization is a naturally occurring process within ultramafic formations under elevated temperatures and pressures. The CO₂-water-rock reaction has also been investigated in Columbia River Basalt Group (CRBG) samples by McGrail et al. (2006), who performed grain-scale experiments to show that

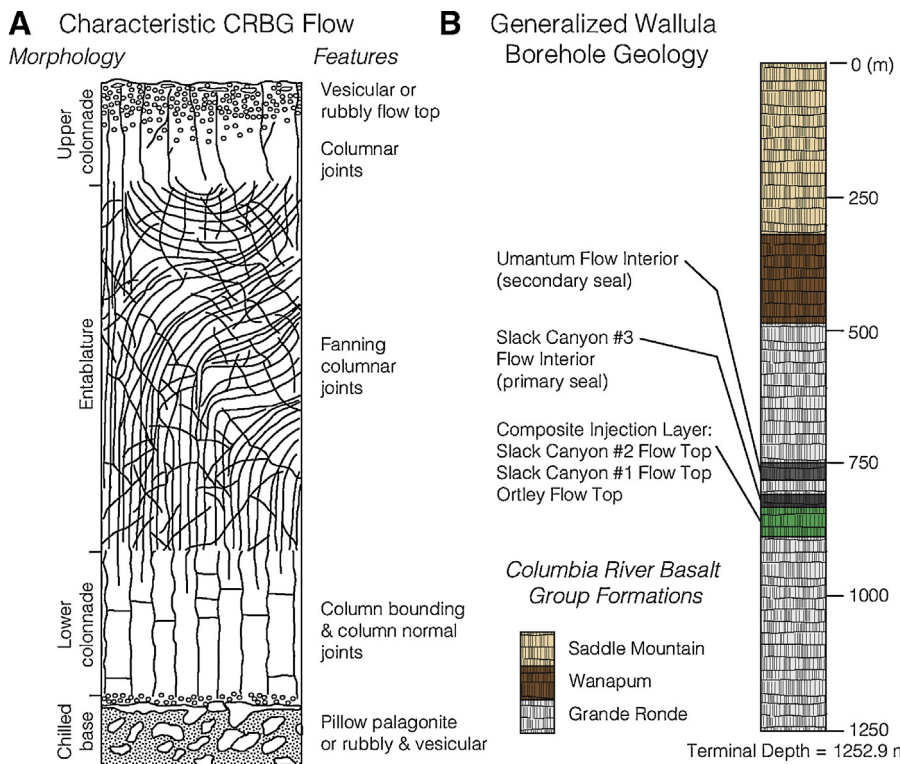


Fig. 1. (A) Schematic illustration of typical flood-basalt flow, modified after Mangan et al. (1986) and McGrail et al. (2010). The vertical dimension ranges from 10^1 to 10^2 m. (B) Generalized illustration of borehole geology from the injection well drilled at the Walulla Basalt Sequestration Pilot Project. The composite injection zone comprises the Slack Canyon #2 flow top (829–844 m bgs), Slack Canyon #1 flow top (853–859 m bgs), and the Ortley flow top (865–874 m bgs) (McGrail et al., 2010).

carbonate mineralization occurs rapidly, on the order of 10^1 to 10^2 days. Building upon this work, Schaefer et al. (2011) found that CO₂ in both the aqueous and supercritical phases produces carbonate precipitates when exposed to CRBG samples under reservoir temperature and pressure for a period of 180 days. Moreover, these experiments demonstrate increasing mineralization rates with increasing temperature and pressure, suggesting favorable conditions for mineralization within deep basalt reservoirs. At the reservoir scale, Aradóttir et al. (2012) used reactive transport simulations for the CarbFix basalt sequestration project to show that 100% of the aqueous phase CO₂ injected during the pilot project is likely to mineralize within 10 years. More recently, geochemical experiments indicate that H₂S impurities within an industrial CO₂ waste stream can be permanently co-sequestered as pyrite (Schaefer et al., 2013), and numerical simulations of this process suggest H₂S concentrations up to 1 mol% do not adversely impact long term CO₂ mineralization (Bacon et al., 2014). To complement these results, CCS in deep basalt reservoirs is motivated to a large extent by the relatively high storage potential within both onshore and offshore basalt formations. Storage estimates in the Columbia River Basalt Group of the northwestern United States are estimated to be on the order of 100 Gt CO₂ (McGrail et al., 2006), and offshore basalt formations within the Juan de Fuca plate and Central Atlantic Magmatic Province hold potential for CO₂ storage on comparable scales (Goldberg et al., 2008, 2010). Perhaps the most significant opportunity for CCS in mafic reservoirs is within India's Deccan Traps, where rapid economic growth is driven primarily by coal-fired electricity generation and storage estimates are on the order of 150 Gt CO₂ (Jayaraman, 2007).

Among the principal challenges for industrial-scale CCS in any geologic environment is to ensure >99% CO₂ isolation per thousand years (USDOE, 2013), which, if not met, will likely postpone rather than mitigate global warming trends (Shaffer, 2010). This criterion is particularly challenging in flood-basalt reservoirs, which

comprise layered assemblages of pervasively fractured basalt flows characterized by (1) densely fractured to rubbly, vesicular flow tops resulting from rapid contraction during cooling, (2) a central entablature (flow interior) comprising narrow aperture, fanning columnar joints with hexagonal cross-sectional geometry, and (3) lower colonnades with vertical column-bounding and, to a lesser extent, horizontal column-normal joints (Fig. 1A) (Mangan et al., 1986; DeGraff and Aydin, 1987; McGrail et al., 2009). Borehole characterization at the Wallula Basalt Sequestration Pilot Project in southeast Washington State revealed permeability values between 10^{-13} and 10^{-14} m² within the vesicular flow tops and 10^{-20} to 10^{-21} m² within flow interiors (McGrail et al., 2009), which suggests that flow interiors may provide a sufficient cap rock seal over the timescales needed for CO₂ isolation through mineralization. Despite these field tests, however, the spatial distribution of *in situ* fracture networks within basalts reservoir at injection depth (>800 m) is a significant source of uncertainty for predictive models of plume behavior (Polleyea and Fairley, 2012; Polleyea et al., 2014). Moreover, the mechanical integrity of basalt reservoirs under long-term injection pressure is a paramount concern because CO₂ injected above background reservoir pressure may result in a number of adverse consequences, including fracture propagation and/or reactivation (Lucier et al., 2006; Goodarzi et al., 2011), shear or joint dilation (Min et al., 2004), induced seismicity (Cappa and Rutqvist, 2011), and cm-scale displacements on small, difficult to characterize faults and fractures (Zoback and Gorelick, 2012). These effects are particularly important within basalt flow interiors, where the fanning geometry of columnar joints suggests that some subset of the fracture network may be optimally aligned for shear dilation and propagation. Additionally, increasing fluid pressure within the central entablature may also result in fracture dilation, which would dramatically increase the effective permeability because discharge within both open and closed fractures is known to

increase with the cube of fracture aperture (Witherspoon et al., 1980).

Injection pressure accumulation and distribution during CO₂ sequestration is an important factor for understanding a number of operational risks, including geomechanical reservoir integrity (NETL, 2011; Rutqvist, 2012), accurate constraints reservoir storage efficiency (Gorecki et al., 2015; Bachu, 2015), and brine migration away from the disposal reservoir (Birkholzer et al., 2015). The spatial and temporal evolution of injection pressure during CCS is most commonly quantified through modeling studies, which have shown that reservoir permeability exerts a first-order control on injection pressure accumulation, see, e.g., Birkholzer et al. (2009), Mathias et al. (2009), and Han et al. (2011). In addition to bulk permeability, the presence of two immiscible phases (scCO₂ and brine) requires knowledge of relative permeability effects within both the disposal reservoir and cap rock formations. Laboratory core-flood experiments have shown that relative permeability within CO₂-brine systems is moderate to highly interfering, i.e., the sum of each phase permeability is less than one (Krevor et al., 2012; Benson et al., 2006; Bennion and Bachu, 2005). In addition, Bennion and Bachu (2006) showed that relative permeability is sensitive to interfacial tension, which is dependent on temperature, pressure, and salinity. This work also demonstrated that CO₂-brine systems exhibits hysteresis in both the wetting and non-wetting phase relative permeability. In numerical models of CO₂ sequestration, relative permeability effects are typically accounted for as a constitutive relationship within the multi-phase formulation of Darcy's Law. In this approach, bulk permeability is scaled for each phase as function of effective wetting phase saturation Nordbotten and Celia, 2012, p. 74–86, and the relative permeability scaling coefficient is computed on the basis of characteristic curves, the most common of which are the van Genuchten-Mualem (Van Genuchten, 1980), Brooks-Corey (Brooks and Corey, 1964), or Corey (Corey, 1954) models. These models are specified with a number of empirical parameters, such as the residual phase saturations, pore size distribution index (Brooks-Corey) or phase-interference parameter (van Genuchten-Mualem), which are typically constrained by fitting one of these models to experimental data.

Although curve fitting to experimental data is a reasonable and defensible method for estimating relative permeability model parameters, there remains uncertainty in the approach. For example, core-scale heterogeneity has been implicated in disagreement between experimental results within different cores from the same geologic formation (Berg et al., 2013). Moreover, very high residual CO₂ saturation (>60%) may arise in experimental results due to the relationship between orientations of sub-core heterogeneities and flow direction within the experimental apparatus (Perrin and Benson, 2010). The uncertainty that arises when translating core-scale experimental results into site-scale numerical modeling studies can manifest itself in a number of ways. For example, Burton et al. (2009) used a 1-D flow model to show a four-fold increase in formation injectivity (permeability × reservoir thickness) and as much as 20% variability in the injection rate due solely to small changes in Brooks-Corey relative permeability parameters. Mathias et al. (2013) improved upon this work by testing a wider range of relative permeability parameter sets and found that formation injectivity varies by as much as ±57% in open reservoirs regardless of bulk permeability; however, these authors also found that formation compressibility is the primary factor governing injectivity in closed reservoirs. Similarly, Han et al. (2011) found that CO₂ plume evolution is strongly governed by residual CO₂ saturation, which is a result supported by Sarkarfarshi et al. (2014).

The complexities associated with relative permeability discussed above are based solely on laboratory and modeling studies in sedimentary basins; where as, comparatively little work has been done to understand the implications of relative permeability

Table 1
Bulk hydrogeologic and thermal reservoir properties.

Property	Symbol	Value	Units
Permeability	k	8.65×10^{-14}	m ²
Porosity	ϕ	0.1	–
Density	ρ_r	2300	kg m ⁻³
Specific heat	c_p	1000	J (kg K) ⁻¹
Thermal conductivity	K_r	1.6	W(m K) ⁻¹

uncertainty in basalt reservoirs. For example, a detailed literature review found just one core-flood experiment investigating relative permeability effects of nitrogen and pure water in a fractured basalt core; however, the authors suggest that their results may be adversely affected by edge effects induced during core fracturing (Bertels et al., 2001). Due to the uncertainty surrounding relative permeability in basalt reservoirs, this study seeks to quantify how variability in relative permeability will influence CO₂ plume configuration, injection pressure accumulation, and far-field pressure distribution. In pursing this objective, a numerical modeling experiment is developed using a simple 1-D radially symmetric domain based on site characterization at the Wallula Basalt Sequestration Pilot Project in southeast Washington State (McGrail et al., 2009). This modeling experiment is designed such that all model properties are held constant with the exception of residual CO₂ saturation (S_{gr}) and the phase interference parameter (λ), which control curvature in the non-wetting and wetting phase relative permeability curves, respectively. CO₂ injection is simulated for 399 unique combinations of S_{gr} and λ , and results show that uncertainty in these parameters can account for a two-fold difference in lateral CO₂ migration distance and >50 MPa of injection pressure.

2. Model development

The Wallula Basalt Sequestration Pilot Project in southeast Washington State completed a 1253 m borehole in April, 2009 (McGrail et al., 2009). Core logs and pumping tests from site characterization delineated a composite injection zone comprising three high permeability (~10⁻¹⁴ m²) basalt flow tops: Slack Canyon #2 (829–844 m bgs), Slack Canyon #1 (853–859 m bgs), and Ortley (865–874 m bgs) (Fig. 1B). This injection zone is bounded above by two low permeability (~10⁻²¹ m²) seals that comprise flow interiors from Slack Canyon #3 (802–829 m bgs) and Umantum flows (744–786 m bgs). The numerical model developed here focuses on the Slack Canyon #2 flow top, which is the thickest of the three flow tops within the composite injection zone.

The Slack Canyon #2 flow top is idealized using the continuum method on the basis that Darcy's Law is valid within the densely fractured and rubbly reservoir rock. In keeping the model aligned with the available pump test data, the Slack Canyon #2 flow top is conceptualized as a single homogeneous layer with 15 m thickness and 100 km lateral extent, which results in a 1-D radially symmetric grid with semi-infinite radial dimension (Fig. 2). The injection well is discretized at the inner boundary as single grid cell with 0.1 m radius. Grid discretization from the injection well to 10,000 m comprises 949 grid cells that increase in width (Δr) logarithmically from 0.001 m adjacent to the injection well to 122 m at 10,000 m. In order to simulate a semi-infinite far-field dimension, an additional 50 grid cells with logarithmically increasing Δr are specified from 10,000 m to 100,000 m. The high resolution grid near the injection well is chosen to minimize discretization effects that create a non-physical pressure spike in early time, as noted by Mathias et al. (2013). The reservoir model is parameterized using data from the Wallula site characterization (Table 1) (McGrail et al., 2009). All boundaries are specified as adiabatic (no flux) on the basis that (1) the Slack Canyon #2 flow top is bounded by flow interiors from the

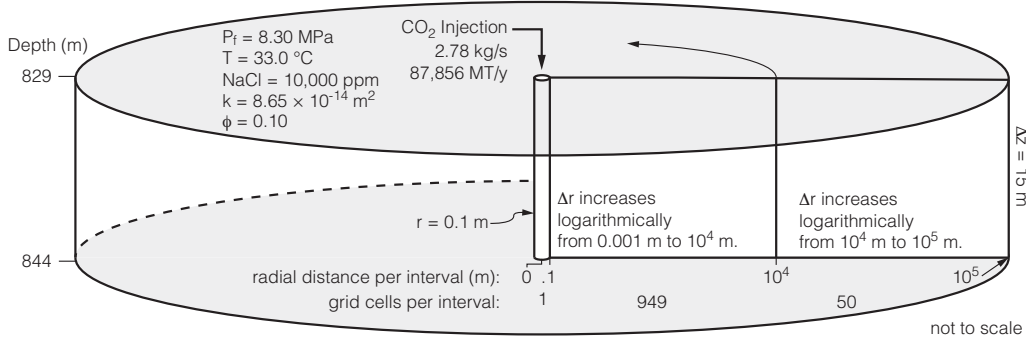


Fig. 2. Schematic illustration of the 1-D radially symmetric model domain used for this study. The injection well is idealized as a single grid cell with 0.1 m radius. The grid cell adjacent to the injection well is specified with a radius of 0.001 m, and the radial dimension of the following 949 grid cells increase logarithmically to 10,000 m, after which 50 logarithmically increasing grid cells are specified to the maximum lateral dimension of 100,000 m.

Slack Canyon #3 (above) and Slack Canyon #2 (below) flows, which have permeability of $4 \times 10^{-21} \text{ m}^2$ and $4 \times 10^{-20} \text{ m}^2$, respectively (McGrail et al., 2009) and (2) the 100 km lateral dimension of the model domain is sufficiently large to simulate an infinite far-field dimension.

Wetting phase relative permeability (k_w) is accounted for using the van Genuchten–Mualem model (Van Genuchten, 1980; Pruess et al., 1999), which for partial saturation is given as:

$$k_w = \sqrt{S_e} [1 - (1 - S_e^{1/\lambda})^\lambda]^2, \quad (1)$$

where λ is the phase interference parameter governing curvature and S_e is effective wetting phase saturation: $(S_l - S_{lr})/(S_{ls} - S_{lr})$. In the expression for S_e , S_l is the wetting phase saturation, S_{lr} is the saturation below which the wetting phase becomes immobile, and S_{ls} is the saturation above which the wetting phase is fully mobile (i.e., no relative permeability effects). Non-wetting phase relative permeability (k_{nw}) is modeled for partial saturation using the Corey (1954) curve, which is given as:

$$k_{nw} = (1 - \hat{S})^2 (1 - \hat{S}^2). \quad (2)$$

In this formulation, \hat{S} is effective non-wetting phase saturation: $\hat{S} = (S_l - S_{lr})/(1 - S_{lr} - S_{gr})$, where S_{gr} is the residual non-wetting phase saturation and governs curvature in non-wetting phase relative permeability model.

A review of experimental results for CO₂-brine relative permeability reveals a wide range of moderate to highly interfering behavior within rocks of the same type and geologic formation. This suggests a high degree of uncertainty in site-scale application of relative permeability models, particularly with respect to the parameters governing curvature. In order to quantify the effects of this uncertainty, a relative permeability parameter set is defined for this study such that end-point wetting phase saturations (S_{lr} and S_{ls}) are held constant while the parameters governing model curvature (λ and S_{gr}) vary systematically over a prescribed range. The relative permeability parameter set developed here covers a wide range of experimental data whereby S_{lr} and S_{ls} are equal to 0.3 and 1.0, respectively, λ varies from 0.1 to 0.99, and S_{gr} varies from 0.01 to 0.50 (Fig. 3). Although Fig. 3 presents the Bertels et al. (2001) relative permeability data for basalt, the non-wetting phase relative permeability parameter space defined here does not overlap with Bertels et al. (2001) data on the basis that the authors indicate edge effects from the induced core fractures may have adversely affected their results. Individual simulations are performed over the resulting parameter space for 399 unique combinations of λ and S_{gr} , which increment at intervals of 0.05 and 0.005, respectively, over the prescribed ranges (Fig. 4). Although capillary pressure will also play a significant role in CO₂ mobility and injection pressure accumulation (Sarkarfarshi et al., 2014), this work seeks to isolate

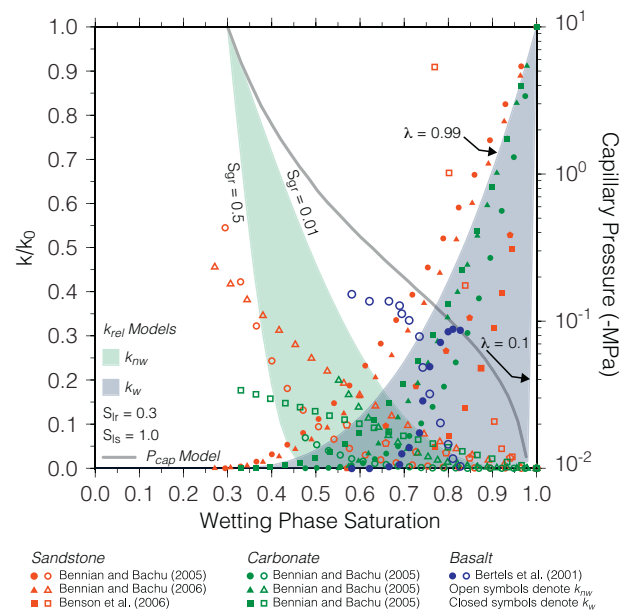


Fig. 3. Range of relative permeability curves used in the present study compared with experimental relative permeability data extant in the literature. Blue shading denotes the range of the van Genuchten–Mualem (1980) wetting phase relative permeability model for λ between 0.1 and 0.99. Green shading denotes the range of the Corey (1954) non-wetting phase relative permeability for S_{gr} between 0.01 and 0.50. Gray curve is the capillary pressure (P_{cap}) model used for this study. (For interpretation of the references to color in this figure legend, the reader is referred to the web version of this article.)

for the effects of relative permeability, and, as a consequence, a generic capillary pressure model is specified and held constant for each simulation run (Fig. 3).

The code selection for this study is an advanced beta version of TOUGH3 (Jung et al., 2015) compiled with ECO2N (Pruess, 2005), which is the fluid property module for simulating non-isothermal mixtures of water, CO₂, and NaCl. For each simulation run, CO₂ is injected into the Slack Canyon #2 flow top for 10 years at constant rate of 2.78 kg s^{-1} ($87,856 \text{ MT yr}^{-1}$) and reservoir temperature of 33.0 °C. This injection rate is 10% of annual CO₂ mass proposed in Case 2 of the Wallula Site Final Scientific/Technical Report (McGrail et al., 2010). The lower injection rate is used on the assumption that highly restrictive relative permeability parameter sets would likely result in fluid pressure approaching or in excess of the thermo-physical correlations for pressure (60 MPa) within the ECO2N fluid property module. Initial conditions for the Slack Canyon #2 flow top are specified on the basis of McGrail et al. (2009) and McGrail et al. (2010) as fully saturated in the wetting phase, where fluid

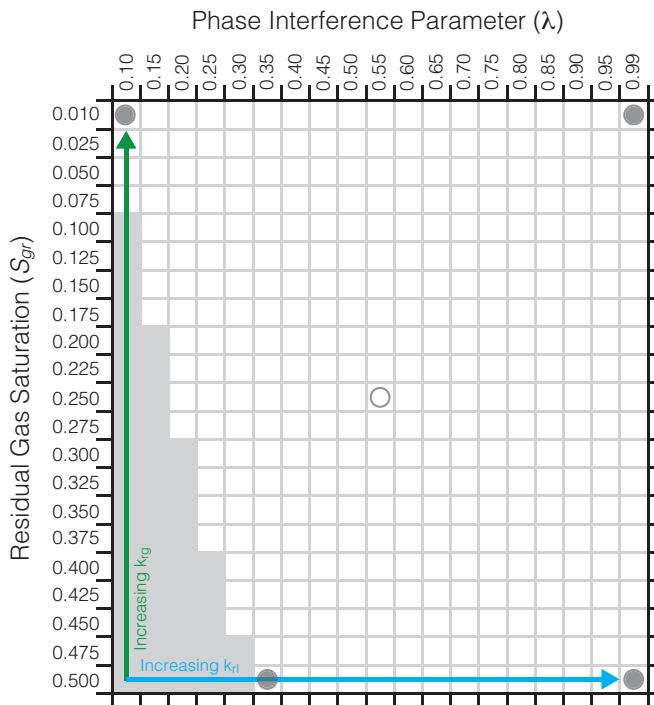


Fig. 4. Schematic illustration of the relative permeability parameters sets used in this study. The phase interference parameter (λ) controls curvature in the van Genuchten-Mualem (1980) wetting phase relative permeability model, and the residual CO₂ saturation (S_{gr}) controls curvature in the Corey (1954) non-wetting phase relative permeability model. Individual simulations are performed for 399 unique combinations of λ and S_{gr} . Gray shading denotes the 46 simulations that did not complete 10 years of simulation time due to excessive pressure build-up. Shaded circles denote parameter sets presented in Figs. 9 and 10. Shaded and open circles denote parameter sets presented in Figs. 6, 9 and 10.

pressure is 8.3 MPa, temperature is 33.0 °C, and salt concentration is 10,000 ppm. In addition, bulk permeability decreases as a function of solid salt precipitation; however, these effects are negligible due to the low brine concentration.

In closing the discussion of model development and parameterization, a brief mention of several simplifying assumptions is warranted. The ensemble of simulations presented here accounts solely for active CO₂ injection, and long term, post-injection CO₂ plume migration is omitted from the analysis. This simplification obviates the need to specify scanning curves for relative

permeability hysteresis because only the drainage phase is modeled. In addition, these numerical simulations neglect the effects of mineral trapping, which would likely influence bulk and relative permeability over time-scales ranging from 10¹ to 10² years (Aradóttir et al., 2012). And finally, increasing fluid pressure may result in fracture/pore dilation, which would increase bulk permeability due to decreasing effective stress; however, this work neglects the hydro-mechanical coupling to describe this behavior. On the basis of these simplifying assumptions, this work is relevant primarily with respect to the mechanical reservoir response in early time, i.e., prior to widespread mineralization. Furthermore, the discussion of results represents a conservative (worst case) geomechanical analysis as fluid pressures would likely lessen as fracture/pore dilate allowing pressure to migrate more rapidly into the far field. As a result, the discussion that follows is limited in extent to early time phenomena, such as pressure-induced reservoir mechanics and plume configuration during injection.

3. Results

A total of 399 individual CO₂ injection simulations were completed within the Slack Canyon #2 flow top while systematically varying the phase interference parameter (λ) and residual non-wetting phase saturation (S_{gr}), which govern curvature in the wetting and non-wetting phase permeability models, respectively. From this ensemble of simulations, 46 (11.5%) failed to reach the specified 10 years of simulation due to pressure accumulation in excess of the TOUGH3/ECO2N thermophysical property table. The λ and S_{gr} parameter combinations that failed are shaded gray in Fig. 4, and represent cases where interference restricts the mobility of each phase to a very small saturation window, i.e., the relative permeability curve for each phase is close to vertical (Fig. 3). This results in rapid pressure accumulation as CO₂ enters the injection well and becomes effectively trapped in the near-field region adjacent to the well due to low non-wetting phase mobility. Similarly, the brine permeability drops rapidly as CO₂ enters the system, which also results in pressure accumulation because the brine cannot be displaced. The massive pressure build-up for cases with extreme phase interference is a consequence of the constant rate CO₂ injection; however, this result implies that reservoir injectivity would be prohibitively low for a constant pressure CO₂ injection.

The 353 simulations to complete the specified 10 years of simulation are combined into individual datasets describing the pressure response and CO₂ plume configuration as functions of λ and S_{gr} . Fig. 5 illustrates the maximum pressure at the injection

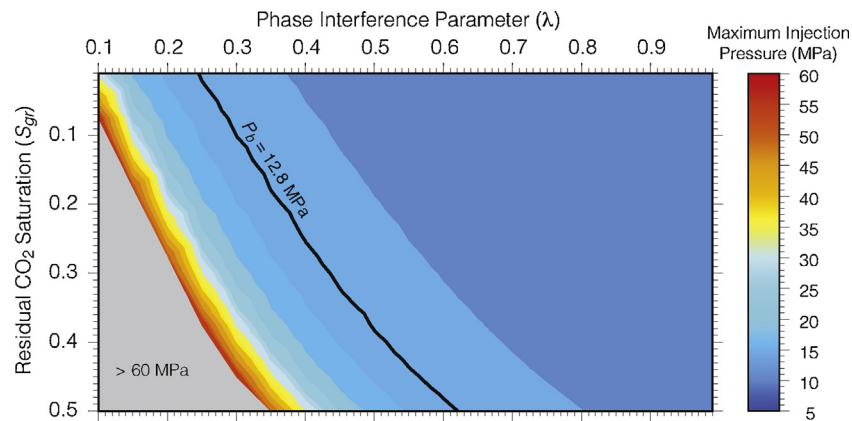


Fig. 5. Pressure response at the injection well as a function of (1) the phase interference parameter (λ), which controls curvature in the van Genuchten-Mualem wetting phase relative permeability model and (2) residual non-wetting saturation (S_{gr}), which controls curvature in the Corey non-wetting phase relative permeability model. Gray shading denotes the parameter space where injection pressure exceeds the TOUGH3/ECO2N pressure limit (60 MPa). The black contour line denotes breakdown pressure (P_b) computed for the Slack Canyon #2 flow top by Eq. (3).

well, which ranges from 10.64 MPa to >60 MPa. In order to assess how maximum injection pressure scales with CO₂ injection rate, an additional suite of simulations was completed for CO₂ injection rates ranging from 8786 to 878,564 MT yr⁻¹, which corresponds with 1–100% of Case 2 CO₂ injection scenario proposed for the Wallula Site (McGrail et al., 2010). The scaling simulations were completed for five λ and S_{gr} parameter combinations within the parameter space (Fig. 4, circles), and results are presented in Fig. 6. The far-field pressure response at 500 m radial distance from the injection well is shown in Fig. 7, which indicates that the maximum fluid pressure ranges from 9.70 MPa to 33.04 MPa. To evaluate the effects of the relative permeability parameter space on plume configuration, the maximum radial extent for CO₂ saturation greater than 0.01 is plotted as a function of λ and S_{gr} . These results are presented in Fig. 8, which illustrate that plume dimension ranges from 595 m to 1203 m in lateral extent. The spatial distribution of reservoir pressure and CO₂ saturation after 10 years of injection are presented in Fig. 9 for λ and S_{gr} parameter combinations bounding the parameter space (Fig. 4, solid circles), and time-series injection pressure for these parameter sets is presented in Fig. 10. These simulations reveal that relative permeability variability can result in dramatic differences in reservoir pressure accumulation and CO₂ plume configuration, and the following discussion relates the effects to CCS risk factors, such as borehole breakdown, far-field reservoir failure, and site monitoring strategies.

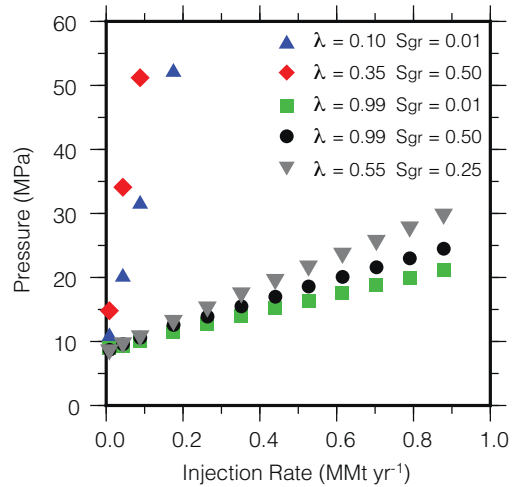


Fig. 6. Maximum injection pressure for four λ and S_{gr} parameter combinations bounding the parameter space (Fig. 4, solid circles), and the λ and S_{gr} combination in the center of the parameter space (Fig. 4, open circle). The maximum CO₂ injection rate is 878,564 MT yr⁻¹, which is the CO₂ injection rate proposed for one scenario at the Wallula site, and would be distributed across multiple flow tops.

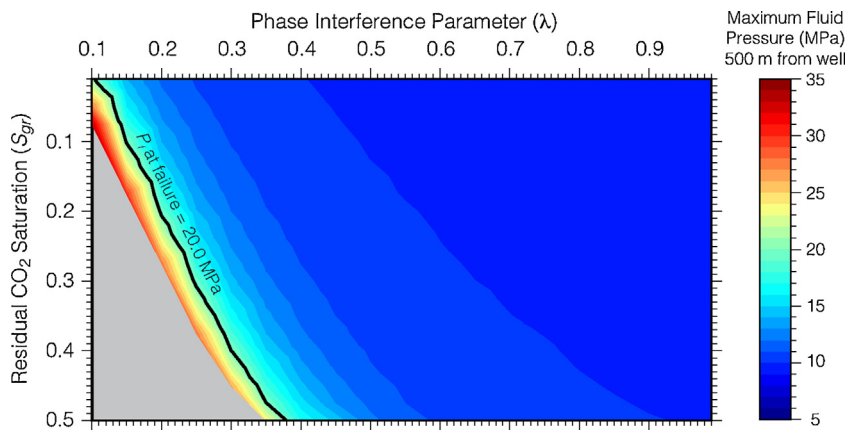


Fig. 7. Far-field fluid pressure response at 500 m radial distance as a function of (1) the phase interference parameter (λ), which controls curvature in the van Genuchten-Mualem wetting phase relative permeability model and (2) residual non-wetting saturation (S_{gr}), which controls curvature in the Corey non-wetting phase relative permeability model. Gray shading denotes the parameter space where simulations failed to complete 10 years of simulation time. The black contour line denotes fluid pressure (P_f) at Mohr failure computed for the Slack Canyon #2 flow top by Eqs. (6) and (7).

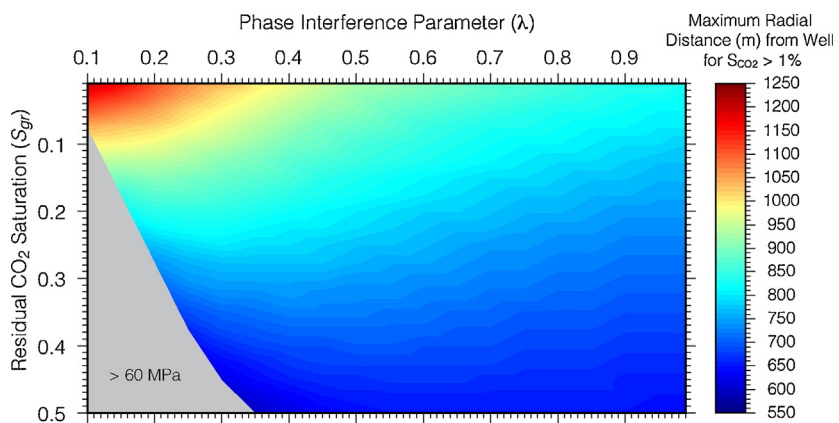


Fig. 8. Response surface for maximum radial distance for CO₂ saturation greater than 0.01 (R_{CO_2}) as a function of (1) phase interference parameter (λ), which controls curvature in the van Genuchten-Mualem wetting phase relative permeability model and (2) residual non-wetting saturation (S_{gr}), which controls curvature in the Corey non-wetting phase relative permeability model. Gray shading denotes the parameter space where simulations failed to complete 10 years of simulation time.

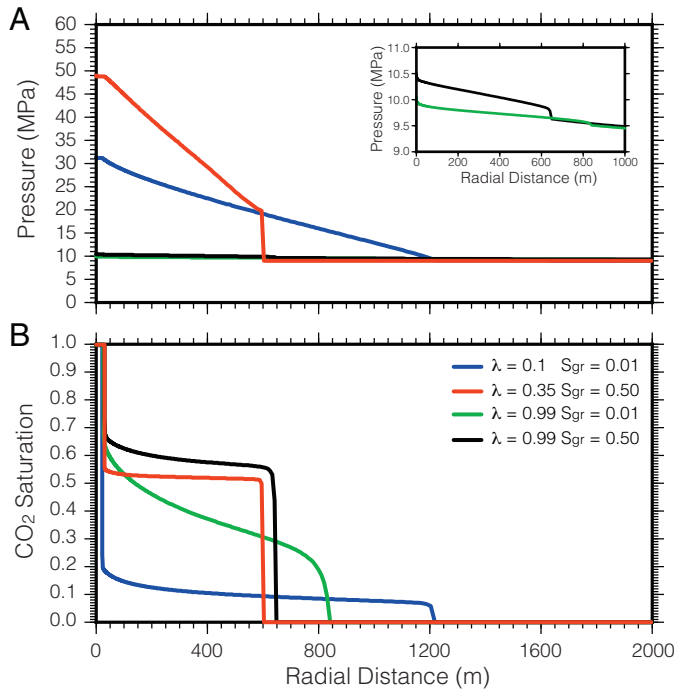


Fig. 9. Pressure (A) and CO₂ saturation (B) simulation results after 10 years of CO₂ injection into the Slack Canyon #2 flow top for relative permeability parameter sets bounding the parameter space (Fig. 4, gray circles). (For interpretation of the references to colour in text, the reader is referred to the web version of this article.)

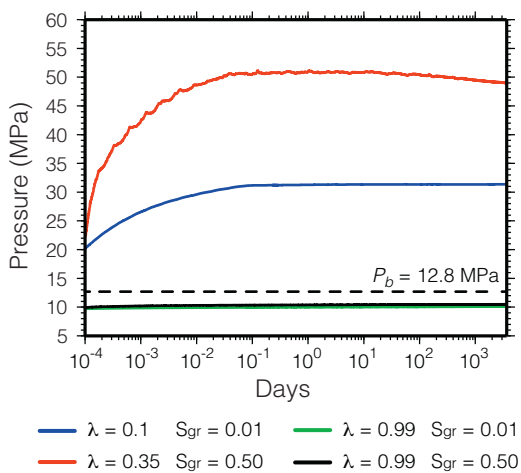


Fig. 10. Time-series pressure at the injection well for relative permeability parameter sets bounding the parameter space (Fig. 4). Dashed line denotes breakdown pressure (P_b) computed by Eq. (3).

4. Discussion

Within the risk profile for CCS in deep geologic formations is the potential for increasing pore fluid pressure to reduce effective stress, which may reactivate existing shear fractures (mode II and III motion) or dilate and propagate joints (mode I motion) (Lucier et al., 2006; Goodarzi et al., 2011; Rutqvist, 2012). As a result, geomechanical reservoir integrity has become an important criterion for numerical model-based risk assessment in CCS reservoir siting (NETL, 2011). Results from the ensemble of CO₂ injection models developed here for the Slack Canyon #2 flow top suggest that uncertainty and/or spatial heterogeneity in reservoir relative permeability may have a profound influence on fluid pressure

Table 2
Mechanical properties for basalt rock mass.

Property	Symbol	Value	Units
Tensile strength	T_0	1.5	MPa
Poisson's ratio	ν	0.3	–
Bulk compressibility	β_i	1.9×10^{-11}	MPa ⁻¹
Fractured compressibility	β_b	4.8×10^{-11}	MPa ⁻¹

Parameters are based on basalt rock mass properties from Schultz (1995).

accumulation, which translates into uncertainty surrounding reservoir failure criteria.

At the borehole scale, tensile failure (hydraulic fracture) is governed by the interactions between radial stress concentrations along the borehole wall, well bore fluid pressure, and the far-field horizontal stresses. Horizontal compressive stresses acting normal to the borehole circumference are deflected 90° as tensile stresses; whereas, horizontal compressive stresses acting tangential to the borehole are magnified 3×. These local scale effects become superimposed on the regional stress field, which results in a criterion for hydraulic fracture (or breakdown) pressure (P_b) given by Jaeger et al. (2009) as:

$$P_b = \frac{3S_h - S_H + T_0 - 2\eta P_f}{2(1 - \eta)} \quad (3)$$

$$\eta = \frac{\alpha(1 - 2\nu)}{2(1 - \nu)} \quad (4)$$

$$\alpha = 1 - \frac{\beta_i}{\beta_b}, \quad (5)$$

where T_0 is the tensile strength, P_f is initial fluid pressure (8.3 MPa), and η accounts for poroelastic effects in a permeable rock mass (Jaeger et al., 2009). This poroelastic term includes the bulk and unfractured rock mass compressibility (β_b and β_i , respectively), Poisson's ratio (ν), and the Biot parameter (α). Although the state of stress has not been measured at the Wallula site, regional tectonic stresses within the Columbia Plateau indicate the maximum compressive stress is horizontal ($\sigma_1 = S_H$) and the minimum compressive stress is lithostatic ($\sigma_3 = S_V$) (Heidbach et al., 2001). In the vicinity of the Wallula Basalt Sequestration Pilot Project, the S_H azimuth ranges between 2° and 23° east of north (Heidbach et al., 2001). Within the Slack Canyon #2 flow top, S_H and S_h are estimated as 60.0 MPa and 27.5 MPa, respectively, by projecting a least-squares fit through *in situ* stress measurements from the Hanford Nuclear Reservation (Fig. 11), which is approximately 60 km northwest of the Wallula site (Paillet and Kim, 1987). Eqs. (3)–(5) are parameterized using mechanical properties for a basaltic rock mass (Schultz, 1995), which are summarized in Table 2. For the Slack Canyon #2 flow top, the application of Eqs. (3)–(5) results in a borehole breakdown pressure, P_b , of 12.8 MPa.

For the model scenario presented here, P_b (Eq. (3)) is mapped into the pressure response surface (Fig. 5), which indicates injection pressure accumulation below the breakdown threshold over ~2/3 of the parameter space. The shape of the pressure response surface is useful for interpreting the relative influence of each parameter on near-field pressure accumulation in the model scenario. The pressure magnitude generally decreases non-linearly with decreasing S_{gr} and increasing λ , and the response surface comprises two distinct features: (1) a steeply dipping region that corresponds with the more restrictive parameter sets ($\lambda \lesssim 0.35$) and (2) a broad, generally flat region where variations in λ and S_{gr} exhibit little influence on injection pressure. Where the pressure response is strongly non-linear, the directional gradients provide an indication of which parameter more strongly influences pressure build-up. In this region of the response surface, the pressure gradient with respect to phase interference ($\partial P/\partial \lambda$) is ~−265 MPa, where as

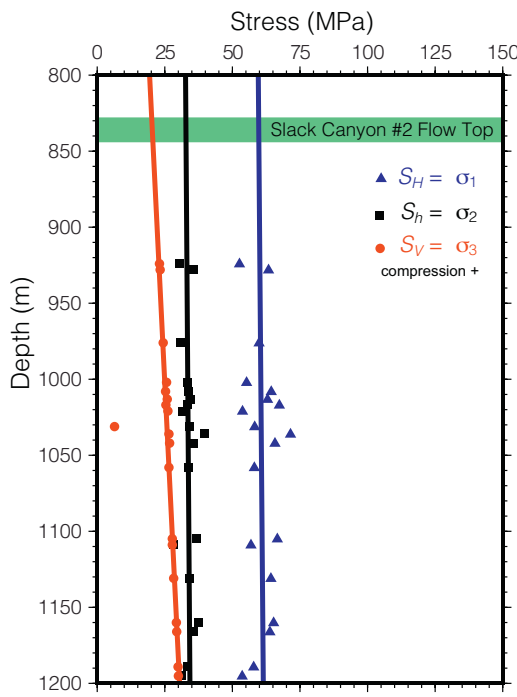


Fig. 11. Regional stress state measured at the Hanford Nuclear Reservation (Paillet and Kim, 1987), which is ~60 northwest of the Wallula Basalt Sequestration Pilot Project site: blue triangles denote maximum compressive horizontal stress (S_H), black squares denote minimum compressive horizontal stress (S_h), and red circles denote lithostatic stress (S_V). Corresponding lines denote linear regression fit to each dataset for projecting the principal stresses to a depth corresponding with the Slack Canyon #2 flow top (green shading). (For interpretation of the references to colour in this figure legend, the reader is referred to the web version of this article.)

the gradient with respect to residual CO₂ saturation ($\partial P/\partial S_{gr}$) is ~153 MPa. Consequently, a unit change in λ results in a proportionately larger change in pressure than a unit change in S_{gr} . This result is supported by time-series injection pressure results for the λ and S_{gr} parameter sets bounding the parameter space (Fig. 10), which show that low values for λ result in very high injection pressure, regardless of S_{gr} . Because λ controls curvature for the wetting phase relative permeability model, this result suggests that brine displacement away from the injection well is a more important factor for injection pressure accumulation than CO₂ mobility into the reservoir.

In order to assess how injection pressure scales with injection rate, an additional suite of simulations was completed with CO₂ injection rates ranging from 8786 to 878,564 MT yr⁻¹, which corresponds with 1–100% of the Case 2 injection scenario proposed in the *Final Scientific/Technical Report* for the Wallula Site (McGrail et al., 2010). These simulations were completed for five λ and S_{gr} parameter combinations within the parameter space, and these parameter combinations are identified with circles in Fig. 4. These scaling results (Fig. 6) indicate that maximum injection pressure generally increases linearly with increasing injection rate for a constant rate injection scenario, and the slope of this scaling relationship is dependent on the selected λ , S_{gr} parameter set. Consequently, this result suggests that maximum injection pressure can be coarsely estimated for a given parameter λ , S_{gr} parameter set on the basis of two simulations with differing injection rates. Additionally, this result suggests that the maximum plausible injection rate for the Slack Canyon #2 flow top is ~263,569 MT yr⁻¹ (30% of the Case 2 Wallula Scenario), beyond which breakdown pressure is reached for the least restrictive λ , S_{gr} parameter combinations. Although this may seem restrictive in terms of CCS implementation in a basalt flow top, it is important to note that CCS in basalt reservoirs

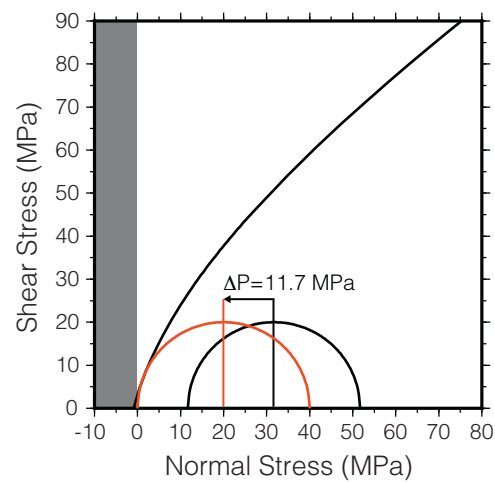


Fig. 12. Shear failure criterion for a basaltic rock mass computed with Eqs. (6) and (7) (Schultz, 1993). Mohr circle in black is defined by the maximum and minimum effective stresses inferred from Fig. 11. Mohr circle in red denotes the effective stress state at failure, which corresponds with a pressure change (ΔP) of 11.7 MPa. Gray shading denotes tensile failure regime, which corresponds with a minimum compressive effective stress of -0.8 MPa.

is predicated upon the delineation of composite injection zones comprising multiple flow tops. Consequently, the scaling results presented here suggest that several basalt flow tops characterized by permeability $\gtrsim 1 \times 10^{-13} \text{ m}^2$ and $\lambda \gtrsim 0.55$ are necessary within the target reservoir to achieve industrial scale implementation.

In addition to borehole scale effects, the propagation of fluid pressure into the reservoir may also lead to shear failure in the far-field as increasing fluid pressure decreases the effective stress acting on optimally aligned faults and fractures. Schultz (1993) developed a shear failure criterion specifically for basaltic rock masses, which accounts for the weakening effects of scale and is given as a Mohr envelope by:

$$\sigma_n = \sigma_3 + \frac{\tau_{\max}^2}{\tau_{\max} + \frac{m\sigma_c}{8}} \quad (6)$$

$$\tau = (\sigma_n - \sigma_3) \sqrt{1 + \frac{m\sigma_c}{4\tau_{\max}}}, \quad (7)$$

where m is an empirical parameter to account for block interlocking within the basalt pile, σ_c is the unconfined compressive strength, and τ_{\max} is $(\sigma_1 - \sigma_3)/2$, for which σ_1 is computed for a rock mass rating of 65 as $\sigma_3 + \sqrt{1651\sigma_3 + 1407}$. Utilizing Schultz (1993) estimates for Columbia River Basalt properties ($m = 6.3$ and $\sigma_c = 262 \text{ MPa}$) with Eqs. (6) and (7) results in the failure criterion presented in Fig. 12. Minimum and maximum effective stresses are computed by subtracting initial porefluid pressure ($P_f = 8.3 \text{ MPa}$) from S_V and S_H , respectively, inferred from Fig. 11, and a standard Mohr circle analysis indicates a pressure change (ΔP) of 11.7 MPa is sufficient to induce shear failure on optimally aligned faults or fractures within the Slack Canyon #2 flow top (Fig. 12). Because the initial reservoir pressure (P_f) within the Slack Canyon #2 flow top is 8.3 MPa, the ΔP of 11.7 MPa is added to P_f indicating that optimally aligned faults and fractures are critically stressed when reservoir fluid pressure reaches 20.0 MPa. The fluid pressure corresponding with Mohr failure is mapped on to the pressure response surface for maximum fluid pressure at 500 m radial distance (Fig. 7). This result indicates that optimally oriented fractures become critically stressed within only ~1/5 of the parameter space corresponding to highly restrictive relative permeability parameter sets, suggesting that uncertainty in relative permeability parameters λ and S_{gr} are unlikely to dramatically influence far-field shear failure for this CO₂

injection scenario. The shape of the far-field pressure response surface shares much resemblance to the injection pressure response (Fig. 5), except that the pressure magnitudes are lower. Within the steeply dipping region of the response surface, the directional gradients, $\partial P/\partial\lambda$ and $\partial P/\partial S_{gr}$, are ~ -114 MPa and ~ 64 MPa, respectively, which suggests that wetting phase relative permeability is a stronger control on far-field pressure build-up than non-wetting phase permeability.

In addition to reservoir geomechanics, the temporal and spatial evolution of CO₂ migration in the disposal reservoir are important criteria for risk assessment. In particular, numerical models of CO₂ injections are commonly used to estimate CO₂ migration, which can influence monitoring, measuring, and verification strategies designed to minimize risks, such as CO₂ leakage from pre-existing faults and/or well bores and brine migration into potable aquifers (NETL, 2011; Birkholzer et al., 2009, 2015). In order to test the influence of relative permeability parameters λ and S_{gr} on the lateral CO₂ plume dimension within the Slack Canyon #2 flow top, a response parameter is defined here as maximum radial distance from the injection well for CO₂ saturation above 0.01 (R_{CO_2}) and plotted against the parameter space (Fig. 8). For the present model scenario, Fig. 8 indicates that variations in relative permeability model curvature can account for a two-fold difference in CO₂ migration distance away from the injection well. The response surface is characterized by a steeply dipping region corresponding with low values of λ and S_{gr} , while the gradient flattens as the parameters increase. Within the steeply dipping region ($\lambda < 0.4$ and $S_{gr} < 0.15$), the directional gradients with respect to phase interference ($\partial R_{CO_2}/\partial\lambda$) and residual CO₂ saturation ($\partial R_{CO_2}/\partial S_{gr}$) are -403 m and -1893 m, respectively, which indicates that residual CO₂ saturation strongly governs radial distance of CO₂ migration away from the injection well (Fig. 8). This result is supported by simulations results for the combinations of λ and S_{gr} bounding the parameter space (Fig. 9B) after 10 years of simulation. In particular, the two bounding cases representing low λ and maximum variability in S_{gr} results in ~ 600 m variation in R_{CO_2} (Fig. 9B, red and blue curves); whereas, the two bounding cases for low S_{gr} and maximum variability in λ results in ~ 350 m difference in R_{CO_2} (Fig. 9B, blue and green curves). In terms of relative permeability effects, this result illustrates that CO₂ mobility is more consequential to CO₂ distribution than λ .

Although S_{gr} is a stronger relative control than λ on CO₂ distribution within the reservoir, the interaction between CO₂ and brine mobility govern the overall plume geometry. When the mobility of each phase is high (low S_{gr} and high λ), CO₂ easily enters the reservoir while brine is readily displaced, resulting in a CO₂ plume characterized by gradually decreasing CO₂ saturation with increasing radial distance from the injection well (Fig. 9B, green curve). Interestingly, the remaining three bounding cases result in a plume configuration characterized by near constant CO₂ saturation over the length of the plume. For the case when CO₂ mobility is high and brine mobility is low (low S_{gr} and low λ), the CO₂ plume is characterized by low and evenly distributed CO₂ saturation over a long radial distance (Fig. 9B, blue curve). This result arises because the CO₂ is highly mobile even at low saturation; however, this low CO₂ saturation is sufficient to induce a high degree of wetting phase interference, which dramatically decreases brine permeability and inhibits brine displacement. As a result, CO₂ migrates long radial distances at very low saturation. One noteworthy facet of this result is the exceptionally high injection pressure required to drive brine migration (Fig. 9A, blue curve), even for the modest CO₂ injection rate (2.78 kg s⁻¹). In contrast, when CO₂ mobility is low (high S_{gr}), the CO₂ plume is characterized by relatively high CO₂ saturation over comparatively small radial distances, regardless of brine mobility (Fig. 9B, black and red curves). These high saturation CO₂ plumes arise because the high S_{gr} results in a steep non-wetting

phase permeability curve that restricts CO₂ mobility to a narrow range of wetting phase saturation slightly above the irreducible wetting saturation. As a result, CO₂ must accumulate to relatively high saturation before the non-wetting phase permeability will permit CO₂ transport (Fig. 9B, black and red curves). Interestingly, this result is independent of injection pressure, as shown in Fig. 9A (black and red curves), which illustrates the pressure distributions for both cases where CO₂ mobility is low. Although relative permeability conditions for each of the four bounding cases is unlikely within a real-world CO₂ disposal reservoir, these results illustrate that relative permeability has potential to strongly influence CO₂ plume configuration.

5. Conclusions

Carbon capture and sequestration development has traditionally focused on deep sedimentary basins; however, mafic reservoirs may also be attractive targets for CO₂ disposal on the basis of permanent mineral trapping over relatively short time scales (10¹–10² yr). Nevertheless, CCS development in mafic reservoirs is hampered by substantial uncertainty in fracture-controlled reservoir characteristics, particularly with respect to the effects of multi-phase fluid flow, e.g., relative permeability and capillary pressure effects. The present study seeks to quantify the uncertainty surrounding relative permeability effects in a basalt reservoir by developing a numerical modeling experiment on the basis of site characterization data from the Slack Canyon #2 flow top, which is one of three flow tops comprising the composite injection zone at the Wallula Basalt Sequestration Pilot Project in southeast Washington State. This numerical modeling experiment controls for the effects of curvature in the relative permeability models by performing an ensemble of 399 CO₂ injection simulations with constant geometry and reservoir properties, while systematically varying the phase interference parameter (λ) and residual CO₂ saturation (S_{gr}), which govern wetting and non-wetting phase relative permeability, respectively. The relative permeability parameter space is defined by selecting combinations of λ and S_{gr} over respective ranges of 0.1–0.99 and 0.01–0.50. For each simulation, CO₂ is injected into the reservoir for 10 years at a constant rate of 2.78 kg s⁻¹ (87,856 MT yr⁻¹), which is 10% of the annual CO₂ utilized in previous modeling studies for the Wallula Site.

Within the Slack Canyon #2 flow top, the ensemble of simulation results show relative permeability alone can account for >50 MPa of variability in the injection pressure and a two-fold difference in lateral CO₂ plume migration, even for the modest injection rate used in this study. The ensemble of results are combined into individual datasets that quantify injection pressure, far-field pressure, and CO₂ plume configuration as functions of λ and S_{gr} . The pressure response surfaces indicate that λ exhibits a stronger control on pressure accumulation than S_{gr} , suggesting that brine displacement governs pressure accumulation at both the injection well and far field scales. Estimates of borehole breakdown pressure and Mohr failure are computed and superimposed on the response surfaces for injection pressure and far-field pressure. This analysis indicates that borehole breakdown is unlikely over $\sim 2/3$ of the parameter space; however, this result applies only to the relatively low injection rate scenario tested here. For higher injection rates, the breakdown pressure would remain unchanged, whereas the injection pressure magnitudes would likely increase resulting in a larger proportion of the parameter space over the failure threshold. Nevertheless, this result implies that injectivity is likely to be favorable for moderate to high phase mobilities. The Mohr analysis indicates that reservoir fluid pressure of 20 MPa is needed to critically stress optimally aligned faults and fracture; however, the pressure response at 500 m radial distance suggests that this is likely

only for the highly restrictive relative permeability parameter sets. Additionally, these results show that non-wetting phase permeability strongly governs CO₂ plume configuration. To describe CO₂ plume configuration, a response variable (R_{CO_2}) is defined as the maximum radial extent for CO₂ saturation above 0.01. Results show that maximum variability in S_{gr} results in ~600 m difference in R_{CO_2} , whereas maximum variability in λ results in ~350 m difference in R_{CO_2} . Moreover, this study finds that interactions between λ and S_{gr} strongly influence overall plume geometry. When both CO₂ and brine mobility are high (low S_{gr} and high λ), the CO₂ plume is characterized by gradually decreasing CO₂ saturation with increasing distance from the injection well. In contrast, when brine mobility is low and CO₂ mobility is high (low λ and low S_{gr}), the CO₂ plume is characterized by very low CO₂ saturation over a large distance from the injection well. For the cases when CO₂ mobility is low (high S_{gr}), the CO₂ plume comprises a comparatively high CO₂ saturation over shorter radial distances, regardless of λ . Moreover, this latter plume configuration is independent of injection pressure, which supports the finding that CO₂ mobility is the primary control on plume geometry.

In closing, this work estimates the bounds of uncertainty associated with relative permeability effects in the Slack Canyon #2 flow top for a modest CO₂ injection rate, while demonstrating a linear relationship between CO₂ injection rate and maximum injection pressure for identically parameterized models. The influence of relative permeability model curvature is shown to have a pronounced effect on both pressure accumulation and CO₂ plume configuration, and this variability becomes increasingly important as CO₂ injection rate increases. Looking forward, there remains significant uncertainty in the application of relative permeability models at reservoir scales. Perhaps the results presented here will spur further investigations in this area, particularly with respect to experimental relative permeability measurements and stress-dependent hydraulic properties in fractured basalts. Lastly, the approach taken here is readily accomplished on modern multi-core desktop computers, and may be suitable for CCS risk assessment at other sites or for uncertainty analysis in different engineered fluid systems, e.g., geothermal reservoir stimulation.

Acknowledgements

This study was funded by the U.S. Department of Energy National Energy Technology Laboratory under contract number DE-FE0023381. The author thanks George Pau for the opportunity to utilize the TOUGH3 numerical modeling code. In addition, the author extends sincere gratitude to Associate Editor Jens Birkholzer and two anonymous peer reviewers for their efforts, the results of which have dramatically improved the quality of this manuscript.

References

- Alexander, G., Mercedes Maroto-Valer, M., Gafarova-Aksoy, P., 2007. Evaluation of reaction variables in the dissolution of serpentine for mineral carbonation. *Fuel* 86 (1), 273–281.
- Aradóttir, E., Sonnenthal, E., Björnsson, G., Jónsson, H., 2012. Multidimensional reactive transport modeling of CO₂ mineral sequestration in basalts at the Hellisheiði geothermal field, Iceland. *Int. J. Greenh. Gas Control* 9, 24–40.
- Bachu, S., 2015. Review of CO₂ storage efficiency in deep saline aquifers. *Int. J. Greenh. Gas Control* 40, 188–202.
- Bacon, D.H., Ramanathan, R., Schaeff, H.T., McGrail, B.P., 2014. Simulating geologic co-sequestration of carbon dioxide and hydrogen sulfide in a basalt formation. *Int. J. Greenh. Gas Control* 21, 165–176.
- Bennion, B., Bachu, S., 2005. Relative permeability characteristics for supercritical CO₂ displacing water in a variety of potential sequestration zones in the Western Canada Sedimentary Basin. In: 2005 SPE Annual Technical Conference and Exhibition. Society of Petroleum Engineers, Dallas, TX.
- Bennion, D.B., Bachu, S., 2006. Dependence on temperature, pressure, and salinity of the IFT and relative permeability displacement characteristics of CO₂ injected in deep saline aquifers. In: 2006 SPE Technical Conference and Exhibition. Society of Petroleum Engineers, San Antonio, TX.
- Benson, S., Tomutsa, L., Silin, D., Kneafsy, T., 2006. Core scale and pore scale studies of carbon dioxide migration in saline formations. In: 8th International Conference on Greenhouse Gas Control Technologies (GHGT-8), Trondheim, Norway.
- Berg, S., Oedai, S., Ott, H., 2013. Displacement and mass transfer between saturated and unsaturated CO₂-brine systems in sandstone. *Int. J. Greenh. Gas Control* 12, 478–492.
- Bertels, S.P., DiCarlo, D.A., Blunt, M.J., 2001. Measurement of aperture distribution, capillary pressure, relative permeability, and in situ saturation in a rock fracture using computed tomography scanning. *Water Resour. Res.* 37, 649–662, Paper Number: 2000WR900316.
- Birkholzer, J.T., Oldenburg, C.M., Zhou, Q., 2015. CO₂ migration and pressure evolution in deep saline aquifers. *Int. J. Greenh. Gas Control* 40, 203–220.
- Birkholzer, J.T., Zhou, Q., Tsang, C.-F., 2009. Large-scale impact of CO₂ storage in deep scaling aquifers: a sensitivity study on the pressure response in stratified systems. *Int. J. Greenh. Gas Control* 3, 181–194.
- Brooks, R., Corey, A., 1964. *Hydraulic Properties of Porous Media*. Hydrology Papers. Colorado State University.
- Burton, M., Kumar, N., Bryant, S.L., 2009. CO₂ injectivity into brine aquifers: why relative permeability matters as much as relative permeability. *Energy Proc.* 1, 3091–3098.
- Cappa, F., Rutqvist, J., 2011. Impact of CO₂ geological sequestration on the nucleation of earthquakes. *Geophys. Res. Lett.* 38, L17313.
- Corey, A., 1954. The interrelation between gas and oil relative permeabilities. *Prod. Monthly*, 38–41.
- DeGraff, J.M., Aydin, A., 1987. Surface morphology of columnar joints and its significance to mechanics and direction of joint growth. *Geol. Soc. Am. Bull.* 99 (5), 605–617.
- GCCSI, 2014. *The Global Status of CCS: 2014*. Global Carbon and Capture Storage Institute, Melbourne, Australia, ISBN:978-0-9871863-5-5.
- Goff, F., Lackner, K., 1998. Carbon dioxide sequestration using ultramafic rocks. *Environ. Geosci.* 5, 89–101.
- Goldberg, D.S., Kent, D.V., Olsen, P.E., 2010. Potential on-shore and offshore reservoirs for CO₂ sequestration in Central Atlantic magmatic province basalts. *Proc. Natl. Acad. Sci. U. S. A.* 107, 1327–1332.
- Goldberg, D.S., Takahashi, T., Slagle, A.L., 2008. Carbon dioxide sequestration in deep-sea basalt. *Proc. Natl. Acad. Sci. U. S. A.* 105, 9920–9925.
- Goodarzi, S., Settari, A., Zoback, M., Keith, D., 2011. A coupled geomechanical reservoir simulation analysis of carbon dioxide storage on the Ohio River Valley. *Environ. Geosci.* 18, 189–207.
- Gorecki, C.D., Ayash, S.C., Liu, G., Braunerberger, J.R., Dotzenrod, N.W., 2015. A comparison of volumetric and dynamic CO₂ storage resource and efficiency in deep saline formations. *Int. J. Greenh. Gas Control* 42, 213–225.
- Han, W.S., Kim, K.-Y., Esser, R.P., Park, E., McPherson, B.J., 2011. Sensitivity study of simulation parameters controlling CO₂ trapping mechanisms in saline formations. *Trans. Porous Media* 90, 807–829.
- Heidbach, O., Tingay, M., Barth, A., Reinecker, J., Kurfeß, D., Müller, B., 2001. World stress map. *Naturwissenschaften* 88, 357–371, release 2008 (accessed 01.02.14).
- Jaeger, J.C., Cook, N.G., Zimmerman, R., 2009. *Fundamentals of Rock Mechanics*, 4th ed. John Wiley & Sons.
- Jayaraman, K., 2007. India's carbon dioxide trap. *Nature* 445, 350.
- Jung, Y., Pau, G., Finsterle, S., 2015. TOUGH3: a new base version of the TOUGH suite of codes. In: *Proceedings of the TOUGH Symposium*. Lawrence Berkeley National Laboratory, Berkeley, CA.
- Kelley, D.S., Karson, J.A., Blackman, D.K., Früh-Green, G.L., Butterfield, D.A., Lilley, M.D., Olson, E.J., Schrenk, M.O., Roe, K.K., Lebon, G.T., Rivizzingo, P., 2001. An off-axis hydrothermal vent field near the Mid-Atlantic Ridge at 30° N. *Nature* 412, 145–149.
- Krevor, S.C.M., Pini, R., Zuo, L., Benson, S.M., 2012. Relative permeability and trapping of CO₂ and water in sandstone rocks at reservoir conditions. *Water Resour. Res.* 48.
- Lucier, A., Zoback, M., Gupta, N., Ramakrishnan, T., 2006. Geomechanical aspects of CO₂ sequestration in a deep saline reservoir in the Ohio River Valley region. *Environ. Geosci.* 13, 85–103.
- Mangan, M.T., Wright, T.L., Swanson, D.A., Byerly, G.R., 1986. Regional correlation of Grande Ronde basalt flows, Columbia river basalt group, Washington, Oregon, and Idaho. *Geol. Soc. Am. Bull.* 97 (11), 1300–1318.
- Mathias, S.A., Gluyas, J.G., González Martínez de Miguel, G.J., Bryant, S.L., Wilson, D., 2013. On the relative permeability data uncertainty and CO₂ injectivity estimation for brine aquifers. *Int. J. Greenh. Gas Control* 12, 200–212.
- Mathias, S.A., Hardisty, P.E., Trudell, M.R., Zimmerman, R.W., 2009. Approximate solutions for pressure buildup during CO₂ injection in brine aquifers. *Trans. Porous Media* 79, 265–284.
- Matter, J.M., Kelemen, P.B., 2009. Permanent storage of carbon dioxide in geological reservoirs by mineral carbonation. *Nat. Geosci.* 2, 837–841.
- McGrail, B., Freeman, C., Beeman, G., Sullivan, E., Wurstner, S., Brown, C., Garber, R., Tobin, D., Steffensen, E., Reddy, S., Gilmartin, J., 2010. *Final Scientific/Technical Report – Capture and Sequestration of CO₂ at the Boise White Paper Mill*. Tech. rep. Pacific Northwest National Laboratory, pNWD-4203.
- McGrail, B., Sullivan, E., Spane, F., Bacon, D., Hund, G., Thorne, P., Thompson, C., Reidel, S., Colwell, F., 2009. *Topical Report – Preliminary Hydrogeologic Characterization Results from the Wallula Basalt Pilot Study*. Tech. rep. Pacific Northwest National Laboratory, pNWD-4129.

- McGrail, B.P., Schaeaf, H.T., Ho, A.M., Chien, Y.-J., Dooley, J.J., 2006. Potential for carbon dioxide sequestration in flood basalts. *J. Geophys. Res.* 111.
- Min, K.-B., Rutqvist, J., Tsang, C.-F., Jing, L., 2004. Stress-dependent permeability of fractured rock masses: a numerical study. *Int. J. Rock Mech. Mining Sci.* 41 (7), 1191–1210.
- NETL, 2010. Best Practices for: Geologic Storage Formation Classification: Understanding its Importance and Impacts on CCS Opportunities in the United States. National Energy Technology Laboratory, dOE/NETL-2010/1420.
- NETL, 2011. Best Practices for: Risk Analysis and Simulation of Geologic Storage of CO₂, 1st ed. National Energy Technology Laboratory, dOE/NETL-2011/1459.
- Nordbotten, J.M., Celia, M.A., 2012. Geological Storage of CO₂: Modeling Approaches for Large-Scale Simulation. John Wiley & Sons, Inc.
- Paillet, F.L., Kim, K., 1987. Character and distribution of borehole breakouts and their relationship to in situ stresses in Deep Columbia River Basalts. *J. Geophys. Res. Solid Earth* 92 (B7), 6223–6234.
- Perrin, J.C., Benson, S., 2010. An experimental study on the influence of sub-core scale heterogeneities on CO₂ distribution in reservoir rocks. *Trans. Porous Media* 82 (1), 93–109.
- Polleyea, R.M., Fairley, J.P., 2012. Implications of spatial reservoir uncertainty for CO₂ sequestration in the east Snake River Plain, Idaho (USA). *Hydrogeol. J.* 20, 689–699.
- Polleyea, R.M., Fairley, J.P., Podgorney, R.K., McLing, T.L., 2014. Physical constraints on geologic CO₂ sequestration in low-volume basalt formations. *Geol. Soc. Am. Bull.* 126 (3/4), 344–351.
- Pruess, K., 2005. ECO2N: A TOUGH2 Fluid Property Module for Mixtures of Water, NaCl, and CO₂. Tech. rep. Lawrence Berkeley National Laboratory, IBNL-57952.
- Pruess, K., Oldenburg, C., Moridis, G., 1999. TOUGH2 User's Guide, Version 2. Tech. rep. Lawrence Berkeley National Laboratory, IGNL-43134.
- Rutqvist, J., 2012. The geomechanics of CO₂ storage in deep sedimentary formations. *Geotech. Geol. Eng.* 30 (3), 525–551.
- Sarkarfarshi, M., Malekzadeh, F.A., Gracie, R., Dusseault, M.B., 2014. Parametric sensitivity analysis for CO₂ geosequestration. *Int. J. Greenh. Gas Control* 23, 61–71.
- Schaeaf, H., McGrail, B., Owen, A., 2011. Basalt reactivity variability with reservoir depth in supercritical CO₂ and aqueous phases. *Energy Proc.* 4, 4977–4984.
- Schaeaf, H., McGrail, B., Owen, A., Arey, B., 2013. Mineralization of basalts in the CO₂-H₂O-H₂S system. *Int. J. Greenh. Gas Control* 16 (0), 187–196.
- Schultz, R., 1995. Limits on strength and deformation properties of jointed basaltic rock masses. *Rock Mech. Rock Eng.* 28 (1), 1–15.
- Schultz, R.A., 1993. Brittle strength of basaltic rock masses with applications to venus. *J. Geophys. Res. Planets* 98 (E6), 10883–10895.
- Shaffer, G., 2010. Long-term effectiveness and consequences of carbon dioxide sequestration. *Nat. Geosci.* 3, 464–467.
- USDOE, 2013. Carbon Technology Program Plan. United States Department of Energy, Washington, DC.
- Van Genuchten, M., 1980. A closed-form equation for predicting the hydraulic conductivity of unsaturated soils. *Soil Sci. Soc. Am.* 44, 892–898.
- Wang, F., Giammar, D.E., 2012. Forsterite dissolution in saline water at elevated temperature and high CO₂ pressure. *Environ. Sci. Technol.* 43, 168–173, May.
- Witherspoon, P., Wang, J., Iwai, K., Gale, J., 1980. Validity of cubic law for fluid flow in a deformable rock fracture. *Water Resour. Res.* 16 (6), 1016–1024.
- Zoback, M., Gorelick, S.M., 2012. Earthquake triggering and large-scale geologic storage of carbon dioxide. *Proc. Natl. Acad. Sci. U. S. A.* 109, 10164–10168.